Monolithic Photonics Using Second-Order Optical Nonlinearities in Multilayer-Core Bragg Reflection Waveguides

Payam Abolghasem, Jun-Bo Han, Dongpeng Kang, Bhavin J. Bijlani, *Student Member, IEEE*, and Amr S. Helmy, *Senior Member, IEEE*

(Invited Paper)

***Abstract*—Recent advancements in phase-matching second-order nonlinear processes by using matching-layer-enhanced Bragg reflection waveguides (ML-BRWs) in $Al_xGa_{1-x}As$ material system are discussed. The limitations on the choice of the $Al_xGa_{1-x}As$ layers for applications that require high pump power operation are highlighted. Multilayer-core ML-BRWs are proposed as a new waveguide design with relaxed constraints over the choice of the $Al_xGa_{1-x}As$ layers composition. The tradeoffs associated with material bandgap on the efficiency of second-order nonlinear processes are examined by using this novel structure. The interplay among the various factors, including the nonlinear overlap factor, the effective second-order nonlinearity, and the third-order nonlinear effects result in the presence of an optimum detuning of the core bandgap from the operating wavelength for maximum conversion efficiency. Two different wafer structures are examined by using second-harmonic generation to elucidate these tradeoffs. The conversion efficiency is examined by using 30-ps, 2-ps, and 250-fs pulses at various pump average power levels.**

***Index Terms*—Bragg reflection waveguides (BRWs), difference-frequency generation (DFG), nonlinear optics, optical nonlinearities in compound semiconductors, phase matching (PM), second-harmonic generation (SHG), sum-frequency generation (SFG).**

I. Introduction

LASERS spawned the quest for the exploration and subsequent utilization of optical nonlinearities. Second-order nonlinearities offer distinct advantages for efficient frequency conversion, quantum-optical applications, and ultrafast all-optical signal processing, and was pursued shortly after lasers were first available [1]. In most practical cases to date, applications that use second-order nonlinear effects are not necessarily amenable to monolithic integration along with other active and passive photonic components. However, monolithic integration could fuel wider adoption and utilization of the capabilities afforded by second-order optical nonlinearities. Most nonlinear optical crystals do not lend themselves to the nanofabrication technologies available for semiconductors, which enable more advanced functionality. Due to significant dispersion, materials with appreciable nonlinearity have the phase velocities of the interacting waves, which relate to how efficiently the nonlinear effects can be utilized, not matched naturally [2]. Matching the phase velocities of the interacting waves has been mastered in several material systems. These include lithium niobate ($LiNbO_3$) [3], potassium titanate phosphate (KTP) [4], and barium borate (BBO) [5]. Techniques such as birefringent-phase-matching and quasi-phase-matching (QPM) have been used to achieve efficient optical sources, ultrafast optical processing elements, and frequency conversion components in these material systems [6]–[8].

Phase matching (PM) in semiconductors was achieved in materials, such as ZnTe and ZnSe, in 1995 [9], [10]. For GaAs, it was achieved initially in 1992 [11] and for InP in 1992 [12]. Nonlinearities of semiconductor materials are generally larger than those for their counterparts, such as KTP, $LiNbO_3$, and BBO while operating near their bandgaps. This benefit is often offset by the enhanced optical losses in semiconductors operating in this regime [13]–[15]. GaAs- and InP-based material systems, despite having higher propagation losses in comparison to other nonlinear crystals, have a well-developed platform for devices, where lasers, modulators, amplifiers, photonic bandgap structure, and other devices have been well developed [16]–[20]. In the case of GaAs compounds, the transparency window is between 0.9–17 μm, compared to 0.5–5 μm for $LiNbO_3$ [21]. GaAs compounds also have higher optical damage thresholds and better thermal conductivity [25]. The integration of second-order nonlinearities with these devices offer distinct functionality and advantages. This, in turn, has driven a great deal of research for efficient PM in compound semiconductors. However, the cubic structure ($\bar{4}3$-m symmetry) of GaAs/$Al_xGa_{1-x}As$ renders these crystals optically isotropic with a lack of intrinsic birefringence. As a result, PM $\chi^{(2)}$ nonlinearities involves significant challenges in these crystals. If PM is achieved effectively in $Al_xGa_{1-x}As$, it can enable the utilization of their large second-order nonlinearity in conjunction with the existing broad base of optoelectronic devices. Numerous techniques have been investigated over the past two decades to phase match the second-order nonlinear processes in $Al_xGa_{1-x}As$. In general, the PM methods can be grouped as either exact PM (EPM) methods

Manuscript received January 10, 2011; revised March 15, 2011; accepted March 16, 2011. Date of publication May 23, 2011; date of current version March 2, 2012. This work was supported by the Natural Sciences and Engineering Research Council of Canada.

P. Abolghasem, D. Kang, B. J. Bijlani, and A. S. Helmy are with the Edward S. Rogers Sr. Department of Electrical and Computer Engineering and the Institute of Optical Sciences, University of Toronto, Toronto, ON M5S 3G4, Canada (e-mail: payam.abolghasem@utoronto.ca; dongpeng.kang@utoronto.ca; b.bijlani@utoronto.ca; a.helmy@utoronto.ca).

J. B. Han is with the Huazhong University of Science and Technology, College of Electrical and Electronic Engineering, 430074 Wuhan, China (e-mail: junbo.han@mail.hust.edu.cn).

Color versions of one or more of the figures in this paper are available online at http://ieeexplore.ieee.org.

Digital Object Identifier 10.1109/JSTQE.2011.2135841

or QPM methods. For EPM, two types have been investigated, namely, form-birefringence PM (FBPM) [22] and modal PM (MPM) [23]. Several QPM methods have also been investigated, including domain-disordered QPM (DD-QPM) [24].

Another technique uses Bragg reflection waveguides (BRWs) or 1-D photonic bandgap structures to attain EPM. Waveguiding in BRWs is carried out through subsequent Bragg reflections at the interface between core and periodic claddings. The devices can be designed such that they additionally support the propagation of bound modes that are formed by total internal reflection (TIR) between a high-index core and periodic claddings with a lower effective index. Utilizing strong modal dispersion properties of propagating modes in a photonic bandgap device, it is possible to achieve EPM in this class of photonics devices. In comparison to other PM techniques in $Al_xGa_{1-x}As$, such as FBPM and QPM, PM by using BRWs benefits from less constraints over the choice of materials. For example, in FBPM devices, the necessity of incorporating AlO_x layers with high absorption above 7.5 μm, along with the absorption of GaAs above 870 nm, limits the operating wavelengths of these devices. Also in QPM waveguides, operation in proximity of material resonances is required for modulating the $\chi^{(2)}$ coefficient. On the other hand, BRWs are further relaxed in the choice of materials, and hence, offer additional flexibility for on-chip frequency-mixing devices. BRWs have several guiding properties that depart from what is expected in conventional TIR waveguides, which have attracted significant interest [26]. The unique birefringence properties of BRWs [27], [28] were utilized to produce novel devices, such as polarization splitters/combiners [29], while their versatile waveguiding properties were used to tailor the spatial profile of their guided modes [30], [31]. BRWs are also attractive for nonlinear propagation, where spatial optical solitons have been studied [32], as well as applications in which nonlinear optical modes have been found to propagate in BRWs that do not support propagation of bound modes in the linear regime [33].

The quarter-wave BRW (QtW-BRW) is a special case in which the cladding layers have an optical thickness equal to one-quarter of the wavelength with respect to the transverse wave vector. This constraint places the complex Bloch wave number in the middle of the Bragg stopband, where its imaginary component has the largest value [26], hence ensuring the most rapid field decay in the claddings and highest confinement in the core. QtW-BRWs are attractive because of their relatively simple design, which is determined by the quarter-wave condition. A comprehensive analysis of QtW-BRWs can be found in [34], where it was proven that the effective index of the fundamental Bragg mode only depends on the operating frequency and the core characteristics, and is independent of the cladding reflectors. This implies that two different sets of Bragg reflectors can yield the same effective index. This unique feature of QtW-BRWs holds for both TE and TM polarizations of the fundamental Bragg mode and can find applications, where modal birefringence of the orthogonal polarizations can be eliminated.

Initial studies of phase-matched BRWs focused on utilizing quarter-wave structures. However, the quarter-wave condition imposes constraints over the waveguide design, which limits the efficiency of these devices in nonlinear frequency conversion. For example, QtW-BRWs exhibit small core dimensions, imposed by the PM condition, resulting in a poor nonlinear overlap factor. Due to the oscillating nature of the Bragg modes, this leads to degradation in the nonlinear conversion efficiency. In [36], matching-layer-enhanced BRWs (ML-BRWs) were introduced, which offer an effective technique to tailor the spatial overlap factor of the interacting modes. ML-BRWs are spatially symmetric structures, where the core is composed of a single dielectric layer separated from identical Bragg reflectors, on either side, by a layer referred to as the matching layer (ML). In this design, the thickness of the ML is a deterministic parameter with discrete values determined from the dispersion equations. It is designed such that the bilayers of the transverse Bragg reflectors (TBRs) satisfy the quarter-wave condition while no constraint over the core thickness is imposed. Thus far, ML-BRW have demonstrated efficient second-harmonic generation (SHG) [35], sum-frequency generation (SFG) [43], and difference-frequency generation (DFG) [49], [50]. In this study, ML-BRWs are further generalized to the case, where the waveguide core is composed of multiple dielectric layers. The employment of a multilayer core offers additional design parameters, which are utilized for tailoring the modal profiles of interacting frequencies, hence optimizing nonlinear interactions. Though our discussion focuses on passive frequency-mixing elements, the analytical tools developed here are general and can be applied to active devices, such as BRW lasers with multiple quantum wells as active region [51], [52].

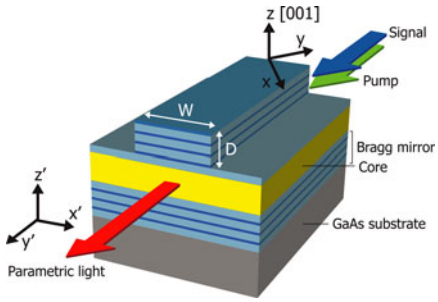

Fig. 1. Schematic of a ridge BRW with ridge width W and etch depth D used for a nonlinear three-mixing process. The coordinate systems of $x'y'z'$ and xyz denote the laboratory and crystal frames, respectively. The two coordinate systems make a rotation angle of $\pi/4$ with respect to the crystal z-axis.

This Article is organized as follows: Section II reviews the second-order nonlinear interactions in AlGaAs waveguides in terms of coupled-mode equations and the tensor properties of $\chi^{(2)}$. Section III provides a review of the characterization of SHG, SFG, and DFG in ML-BRWs, where the limitations in the performance of these devices is highlighted. The analytical tools for the investigation of multilayer-core ML-BRW structures are developed in Section IV. Section V provides the simulation results, device description, and characterization of a multilayer-core ML-BRW that is suited for high-power operation. Conclusions are then presented in Section VI.

II. $\chi^{(2)}$ Nonlinear Interactions in AlGaAs BRWs

A representative BRW is schematically shown in Fig. 1, where the coordinate systems of xyz and $x'y'z'$ denote the crystal and

laboratory frames, respectively. The two reference frames are rotated by an angle of $\phi = \pi/4$ with respect to the crystal z-axis. The choice of $x'y'z'$ reference frame is intended to simplify the analysis of optical mode propagation, where the major fields of TE and TM propagating modes are aligned with the axes of the laboratory frame.

Consider a second-order nonlinear process, where a pump (p) at angular frequency ω_p and a signal (s) at ω_s collinearly interact to generate an idler (i) at ω_i. The propagation direction of interacting modes is taken along the y'-axis. In the presence of optical nonlinearities, the spatial-temporal dependence of the mode at ω_σ, $\sigma \in \{p, s, i\}$, is expressed as

$$\mathbf{E}_{\omega_\sigma}(x', y', z', t) = A_{\omega_\sigma}(y')\mathbf{E}_{\omega_\sigma}(x', z')\exp[i(\beta_{\omega_\sigma} y' - \omega_\sigma t)] \tag{1}$$

where β_{ω_σ} is the propagation constant, ω_{ω_σ} is the angular frequency, $A_{\omega_\sigma}(y')$ is the slowly varying amplitude, and $\mathbf{E}_{\omega_\sigma}(x', z')$ is the spatial profile. Assuming that scalar wave equations are sufficiently accurate in expressing the propagation of optical modes of the pump, signal, and idler, and using the orthogonality relation of optical modes in a guided-wave structure, the coupled-mode equations expressing the spatial variation of field amplitude is derived as [54]

$$\frac{\partial A_{\omega_\sigma}}{\partial y'} = \frac{i\omega_\sigma}{4}\iint E^*_{\omega_\sigma}(x', z')P_{\mathrm{NL}}\exp(-i\beta_{\omega_\sigma} y')dx'dz' \tag{2}$$

where P_{NL} is the nonlinear electric polarization vector. It should be stressed that in (2), $E^*_{\omega_\sigma}(x', z')$ in the integral is represented in the coupled-mode equation as the transverse field profile of the ω_σ mode in the linear regime and its spatial dependency along the propagation direction does not include the slowly varying envelope function. However, in expanding $P^{(\mathrm{NL})}$ in terms of electric fields, variations of the field amplitudes along the propagation direction should be included in the calculations.

In the xyz crystal frame of $\mathrm{Al}_x\mathrm{Ga}_{1-x}\mathrm{As}$, the only independent second-order susceptibility tensor element is $\chi^{(2)}_{xyz}$ and overall six elements [58]. The other nonzero elements are those where the coordinates have been interchanged with all permutations. This implies that nonlinear interaction can only take place when interacting harmonics have nonvanishing field components along all three crystal axes. The elements of the susceptibility tensor in the laboratory and crystal frames are related to each other by using the transformation [58]:

$$\chi^{(2)}_{\mu'\alpha'\beta'} = R_{\mu'\mu}(\phi)R_{\alpha'\alpha}(\phi)R_{\beta'\beta}(\phi)\chi^{(2)}_{\mu\alpha\beta} \tag{3}$$

where $R_{j'j}(\phi)$ are the elements of the rotation matrix with the rotation angle of $\phi = \pi/4$. Using (3), the nonzero elements of $\boldsymbol{\chi}^{(2)}$ tensor in the $x'y'z'$ frame are

$$\chi^{(2)}_{x'x'z'} = \chi^{(2)}_{x'z'x'} = \chi^{(2)}_{z'x'x'} = +\chi^{(2)}_{xyz} \tag{4a}$$

$$\chi^{(2)}_{y'y'z'} = \chi^{(2)}_{y'z'y'} = \chi^{(2)}_{z'y'y'} = -\chi^{(2)}_{xyz}. \tag{4b}$$

Unlike in the crystal frame, where $\chi^{(2)}_{\mu\alpha\beta}$ is nonzero when μ, α, and β are all different, from (4), it can be seen that in the laboratory coordinate system, $\chi^{(2)}_{\mu'\alpha'\beta'}$ is nonzero for those permutations of x', y', and z', where two indexes are identical while the third index is z'.

Due to the zinc-blend crystal structure of $\mathrm{Al}_x\mathrm{Ga}_{1-x}\mathrm{As}$, there exist two distinct growth directions, which allow one to access $\chi^{(2)}_{xyz}$ coefficients. These are the $[0\,0\,1]$ and $[1\,1\,1]$ directions. The growth direction of $[1\,1\,1]$ is usually not desired for planar integrated devices, where waveguides with parallel facets are required. In this case, cleaving the wafer results in waveguides, where the facets make an angle of 60° with respect to each other. Despite this, the $[1\,1\,1]$ growth direction favors surface-emitting nonlinear devices, where the effective second-order nonlinearity is the highest [59]. Devices with $[0\,0\,1]$ growth direction and $[\bar{1}\,1\,0]$ cleavage planes are the most widely used configurations for nonlinear interaction in $\mathrm{Al}_x\mathrm{Ga}_{1-x}\mathrm{As}$ waveguides (see Fig. 1). Three types of nonlinear interactions arise from the nonvanishing susceptibility tensor elements for $[0\,0\,1]$ growth devices. For example, for SHG, these include type-0 interaction, where a pump TM polarization state generates a TM-polarized second-harmonic [37], type-I interaction, where a TE-polarized pump generates a TM-polarized second-harmonic, and type-II interaction, where a pump with hybrid TE + TM polarization generates a TE-polarized second-harmonic. Among these, the type-II process is known to be the most efficient, as it benefits from a larger effective second-order nonlinearity.

For SHG, SFG, and DFG processes, the power of the parametric light, P_{ω_σ}, $\omega_\sigma \in \{\mathrm{SH}, \mathrm{SF}, \mathrm{DF}\}$, follows the relation $P_{\omega_\sigma} \propto d^2_{\mathrm{eff}}\xi^2 L^2$, where L is the device length, d_{eff} is the effective nonlinear coefficient of the structure, and ξ is the nonlinear spatial overlap factor, which are defined as

$$d_{\mathrm{eff}} = \frac{\iint E^*_{\omega_\sigma} d(x', z')E_{\omega_p}E_{\omega_s}dx'dz'}{\iint E^*_{\omega_\sigma}E_{\omega_p}E_{\omega_s}dx'dz'} \tag{5}$$

$$\xi = \frac{\iint E^*_{\omega_\sigma}E_{\omega_p}E_{\omega_s}dx'dz'}{\left(\iint |E_{\omega_\sigma}|^2dx'dz' \iint |E_{\omega_p}|^2dx'dz' \iint |E_{\omega_s}|^2dx'dz'\right)^{1/2}}. \tag{6}$$

In (5), $d(x, y)$ denotes the spatial dependence of effective $\boldsymbol{\chi}^{(2)}$ coefficient in the transverse plane, which is a function of aluminum concentration at a given frequency.

Enhancement of P_{ω_σ} can be carried out by increasing the device length, by enhancing the structure d_{eff}, and by improving the nonlinear overlap factor. In practice, benefits arising from an increase in the device length are offset by the corresponding enhancement of the propagation losses. In order to increase P_{ω_σ}, designs with improved d_{eff} and ξ are desired. In [35], we introduced ML-BRWs, which focused on improving ξ in a SHG experiment by enhancing the generated SH power without aiming to increase the structure d_{eff}. ML-BRW is a simple yet efficient technique for PM $\boldsymbol{\chi}^{(2)}$ processes. The following section provides a review of the recent results of frequency conversion obtained by using ML-BRWs.

III. Frequency Conversion in ML-BRWs

Initial theoretical and experimental endeavors in phase-matching $\boldsymbol{\chi}^{(2)}$ interactions in BRWs utilized QtW-BRWs [60], [61]. Operating at the quarter-wave condition has several advantages, including fastest exponential decay of the Bragg mode in TBRs, simplicity of design equations, polarization degeneracy of the fundamental Bragg mode, and versatile dispersion

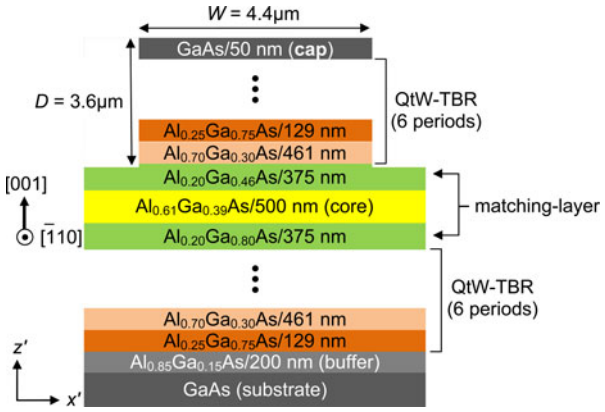

Fig. 2. Epitaxial structure of the BRW_I device. The ML separates the core from the top/bottom QtW-TBRs.

properties. However, phase-matched QtW-BRWs inherit small core dimension of a few hundreds of nanometers, which is dictated by the PM condition. Devices with such small core thicknesses severely suffer from degraded confinement factor and poor end-fire coupling efficiency. Moreover, the deterministic core thickness in phase-matched QtW-BRWs eradicates the flexibilities in tailoring waveguide dispersion while maintaining PM condition. The aforementioned disadvantages in using standard quarter-wave stacks suggest the necessity for investigating more elaborate designs. ML-BRW was a simple design, which was proposed to relieve the constraints over the core dimensions in QtW-BRWs [35], [36]. In this design, the waveguide core thickness is regarded as an independent design parameter while the characteristics of the ML, including its material index and thickness, are used to align the effective-mode index such that the bilayers of TBRs become quarter-wave thick. In the resulting design, one can benefit from a phase-matched BRW with relaxed core dimension while taking advantage of all assets of quarter-wave stacks. In the following sections, we discuss the design and characterization of ML-BRW for PM second-order nonlinearity.

The epitaxial structure of the fabricated ML-BRW, referred to as BRW_I, is shown in Fig. 2. In this design, the ML separates the waveguide core from the top and bottom quarter-wave TBRs (QtW-TBRs). The wafer of BRW_I was grown on nominally undoped $[0\,0\,1]$ GaAs substrate by using metal–organic chemical vapor deposition (MOCVD). Ridge structures were patterned by using plasma etching. The ridge width (W) and depth (D) of BRW_I were 4.4 and 3.6 μm, respectively, with a device length (L) of 1.5 mm.

Linear properties of BRW_I were extracted by using the Fabry–Pérot technique with a single-mode tunable laser around 1550 nm. Linear propagation losses of TE ($\alpha_p^{(\mathrm{TE})}$) and TM ($\alpha_p^{(\mathrm{TM})}$) propagating pump modes were estimated to be 2.0 and 2.2 cm^{-1}, respectively. The input coupling coefficient (C) defined as the spatial overlap factor between the incident pump beam and the lowest order excited TIR mode was determined to be 0.49 with a facets reflectivity (R) of 0.28.

Nonlinear characterization of BRW_I was carried out for pulsed SHG, continuous-wave (CW) SFG, and pulsed/CW DFG. The experimental results are discussed in the following.

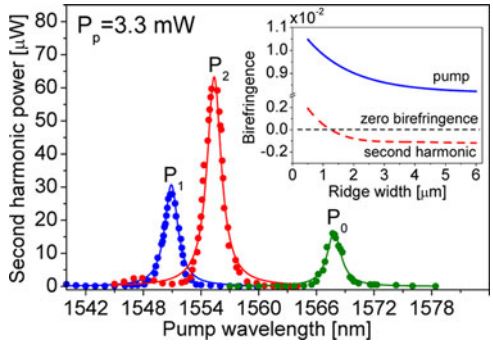

Fig. 3. Second-harmonic average power as a function of pump wavelength measured for three PM schemes. The solid lines are the Lorentzian fit to the measured date. P_0, P_1, and P_2 denote the PM points for type-0, type-I, and type-II SHG, respectively. (Inset) Simulated modal birefringence of pump (solid line) and second-harmonic (dashed line) as functions of the waveguide ridge width. The crossing point between the modal birefringence of SH with the zero birefringence (dotted line) indicates a design for which the SH mode is polarization degenerate.

TABLE I
SUMMARY OF OBSERVED SHG INTERACTIONS IN BRW_I

PM scheme	θ [rad]	P_p [mW]	P_{SH} [μW]	$\bar{\eta}_{SHG}$ [$\%\mathrm{W}^{-1}\mathrm{cm}^{-2}$]
Type-0	0	3.3	16	2.84×10^3
Type-I	$\pi/2$	3.3	28	5.30×10^3
Type-II	$\pi/4$	3.3	60	1.14×10^4

A. Second-Harmonic Generation

SHG in BRW_I was carried out in an end-fire rig setup, thus using a mode-locked Ti:Sapphire pumped optical parametric oscillator (OPO). The employed pulses had a temporal width of 1.8 ps with a repetition rate of 76 MHz. The pulses were nearly transform limited with a temporal–spectral bandwidth product of $\Delta\tau\Delta\nu = 0.53$. A $40\times$ diode objective lens was used at the input stage to couple light into the waveguide. The emerging signal was collected by using a $40\times$ objective lens. A long wavelength pass filter was used in the output stage to separate the pump from the second harmonic. We examined the type-0 [37], type-I, and type-II [35] SHG. The average pump power before the front facet of the device was measured to be 9.6 mW with an estimated internal value of $P_p = 3.3$ mW. The SHG tuning curves of the three PM schemes, obtained by monitoring the SH average power P_{SH}, as a function of the pump wavelength, are shown in Fig. 3. In this figure, the resonance features at points P_0, P_1, and P_2 denotes the pump wavelengths at which PM condition for type-0, type-I, and type-II SHG were satisfied. A summary of the SHG experiment with BRW_I device is given in Table I, where θ denotes the angle between the pump electric field and the z crystal axis, and $\bar{\eta}_{SHG} = P_{SH}/P_p^2 L^2$ is the normalized nonlinear conversion efficiency.

In Fig. 3, the resonance feature at P_0 appearing to the type-0 PM of $TM_\omega \rightarrow TM_{2\omega}$ with the observed SH power level is noteworthy. The $TM_\omega \rightarrow TM_{2\omega}$ interaction has been previously reported in asymmetric multiple-QW waveguides, where the broken symmetry of the structure along the crystal z-axis induced a weak susceptibility tensor element $\chi_{zzz}^{(2)}$ [24], [38]. In the BRW_I structure, isotropic semiconductors were utilized. The source of $TM_\omega \rightarrow TM_{2\omega}$ interaction is not due to the appearance

of $\chi^{(2)}_{zzz}$ element. Rather, it is ascribed to the characteristic of the TM_ω propagating mode, where the pump electric field has a nonzero component along the propagation direction [37].

Also in Fig. 3, the close proximity of the observed PM wavelengths is remarkable. The PM wavelengths of all three interactions were within a spectral window as small as 17 nm. This spectral range lies within the spectral bandwidth of typical ultrashort pulses with temporal widths of a few hundred femtoseconds. In practice, this PM wavelengths proximity can be attractive for several applications. Examples include on-chip sources of photon pairs, where controlling the polarization entanglement is the major interest and generation of wideband SHG with mixed polarization state by using a femtosecond pulsed pump. The small birefringence of the second-harmonic mode played a pivotal role in obtaining the PM wavelengths of all three nonlinear interactions discussed above in proximity of each other. For a propagating mode at ω_σ, the modal birefringence is defined as $\Delta\bar{n}_{\omega_\sigma} = \bar{n}^{(\mathrm{TE})}_{\omega_\sigma} - \bar{n}^{(\mathrm{TM})}_{\omega_\sigma}$, where $\bar{n}^{(\mathrm{TE})}_{\omega_\sigma}$ and $\bar{n}^{(\mathrm{TM})}_{\omega_\sigma}$ are the effective indexes of TE and TM propagating modes, respectively. In the inset of Fig. 3, we have plotted the simulated modal birefringence for both the SH mode (Bragg mode) and the pump mode (TIR mode) as functions of the waveguide ridge width W (see Fig. 1). From the figure, the simulated birefringence at SH is approximately an order of magnitude smaller than that of the pump for the entire simulated value of W. Moreover, there exists a waveguide design for which the polarization degeneracy condition can be fulfilled. The small modal birefringence in addition to the existence of polarization degenerate design is a unique characteristic of BRWs, which deserves further investigation and can find potential applications involving linear and nonlinear effects.

B. Sum-Frequency Generation

SFG is attractive for some nonlinear applications, such as photon up-conversion to the near-infrared regime (600–800 nm) where efficient, low-noise, single-photon detectors are present [39], [40]. Another application is high-speed optical sampling [41], [62] by using ultrashort pulses for waveform measurements and demultiplexing of time-domain multiplexed optical signals [42]. We characterized the $\mathrm{BRW_I}$ device for type-II CW SFG [43] with the pump and signal within the C-band telecommunication wavelength range. A drawing of the apparatus used for SFG characterization is shown in Fig. 4.

For an SFG device, the quantum efficiency η_q is expressed as $\eta_q = P_i\lambda_i/(P_s\lambda_s)$ [40]. For $\mathrm{BRW_I}$, we estimated η_q as a function of the pump power, as illustrated in Fig. 5(a) for a signal with 0.35 mW internal power. The device maximum quantum efficiency was measured to be 0.029%, which was obtained for a pump and signal with internal powers of 4.15 and 0.35 mW, respectively. The associated internal SF power was estimated to be $\approx$0.20 μW. A merit which determines the performance of an SFG device is the 100% quantum efficiency, which is defined as the pump power P_p^{100}, for which η_q is equal to unity. We estimated a required pump power of 14 W for a quantum efficiency of 100%. In practice, other factors, such as heat generation and two-photon absorption (2PA) may further increase this power value. Considering the short-waveguide length, this leaves ample room for decreasing P_p^{100}, provided that propagation losses

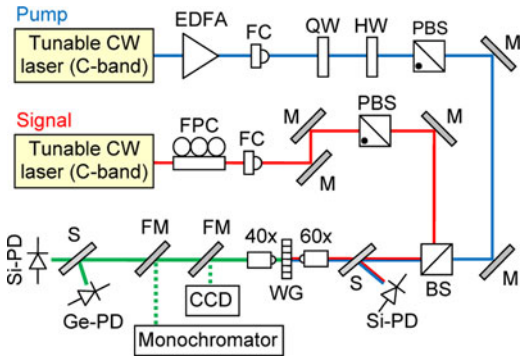

Fig. 4. Schematic of SFG experimental setup. EDFA: fiber amplifier; FPC: fiber polarization controller; FC: fiber collimator; QW: quarter-wave plate; HW: half-wave plate; PBS: polarization beam splitter; BS: beam splitter; S: beam sampler; M: mirror; WG: waveguide; FM: flip mount; Si-PD: silicon photodetector; Ge-PD: germanium photodetector.

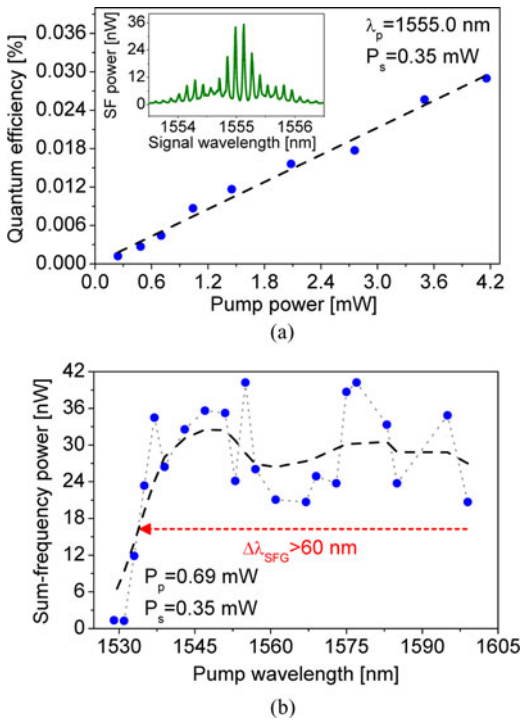

Fig. 5. (a) Quantum efficiency as a function of pump power. Filled circles are the measured data, while the dashed line is the linear fit. Inset: Sum-frequency power as a function of signal wavelength obtained experimentally. (b) Sum-frequency power as a function of pump wavelength. The filled circles are the measured data, while the dashed line is a smoothed fit to remove cavity resonance effect. The pump wavelength range limited the tunability on the long wavelength side.

can be minimized. For example, P_p^{100} can be reduced to 690 mW for a device length of 10 mm. The normalized conversion efficiency of SFG is defined as $\bar{\eta}_{\mathrm{SFG}} = P_i/(P_pP_sL^2)$. For $\mathrm{BRW_I}$, $\bar{\eta}_{\mathrm{SFG}}$ was estimated to be $298\%\mathrm{W}^{-1}\cdot\mathrm{cm}^{-2}$. This suggests that the devices described here have the potential to detect single photons with further optimization, particularly by means of reducing propagation losses [44]. The inset of Fig. 5(a) shows the tuning curve of the SFG experiment, which was obtained by monitoring the SF power as a function of signal wavelength. In obtaining the experimental curve, the internal average powers

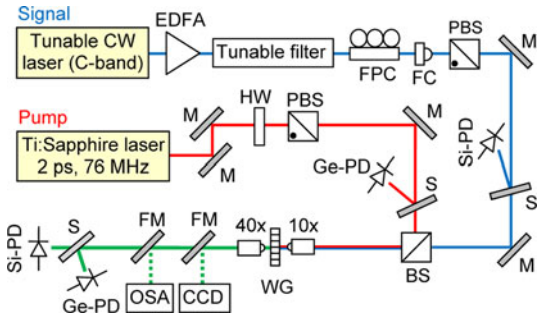

Fig. 6. Schematic of DFG experimental setup. EDFA: fiber amplifier; FPC: fiber polarization controller; FC: fiber collimator; HW: half wave plate; PBS: polarization beam splitter; BS: beam splitter; S: beam sampler; M: mirror; WG: waveguide; FM: flip mount; Si-PD: silicon photodetector; Ge-PD: germanium photodetector.

of pump and signal were 1.98 and 1.00 mW, respectively. From the figure, the distinguishable SF power around 1555 nm with a power level of 35 nW was an indication of phase-matched process. The fast oscillating component on the spectrum indicates the resonance effects of the waveguide cavity at both signal and sum-frequency wavelengths.

The PM bandwidth $\Delta\lambda_{\mathrm{SFG}}$ is a key parameter for an SFG device. For $\mathrm{BRW_I}$, we determined $\Delta\lambda_{\mathrm{SFG}}$ by detuning the pump wavelength from the degenerate wavelength of 1555.0 nm, while the signal wavelength was varied to maximize the generated SF power. The result is shown in Fig. 5(b). The large variation in the data was caused by the modulation of Fabry–Pérot resonance of signal and SF wave. Broadband PM was obtained around 1550 nm with a full-width at half-maximum (FWHM) bandwidth exceeding 60 nm. The real bandwidth is believed to exceed 60 nm, as the available pump source tunability prevented extending the wavelength beyond 1600 nm. This feature can be further enhanced through appropriate design of the BRW properties to provide a widely spaced signal and pump with respect to the sum-frequency [45]. This will, in turn, facilitate the spectral filtering of parasitic second- harmonic of pump/signal from the sum-frequency wave required for practical up-conversion applications in integrated single-photon detection [39], [40].

C. Difference-Frequency Generation

DFG is an attractive technique for the generation of widely tunable coherent infrared radiation, where no appropriate laser medium exists [46]–[48]. We characterized $\mathrm{BRW_I}$ for type-II DFG by using a pulsed pump and a CW signal [49], [50]. The apparatus of the DFG experiment is schematically shown in Fig. 6.

The dependence of the DF average power (P_{DF}) on the pump wavelength, for $\lambda_s = 1546$ nm, is shown in Fig. 7(a), where filled circles show the measured data and the solid-line is a Lorentzian fit. In obtaining the figure, the average powers of pump (P_p) and signal (P_s), measured before the front facet of the waveguide, were fixed to 62.9 and 2.9 mW, respectively. From the experiment, peak DF power of 0.95 nW, estimated right after the output facet of the waveguide, was obtained for the phase-matched pump at 777.8 nm. The bandwidth of the process was found to be 0.48 nm.

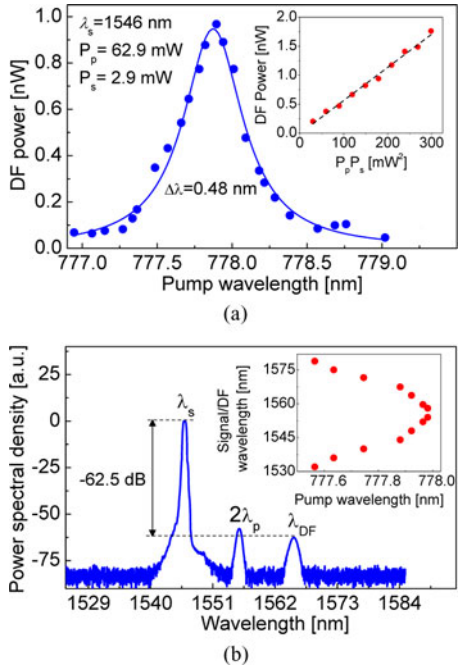

Fig. 7. (a) Variation of the difference-frequency average power as a function of pump wavelength for $\lambda_s = 1545.9$ nm. Filled circles are the measured data and the solid line is the Lorentzian fit. Inset: Dependence of P_{DF} on P_pP_s. Open circles are the measured data, while the dashed line is a linear fit.

In a DFG process, P_{DF} is proportional to the product of pump and signal powers. We verified this relation for a fixed pump power of 62.9 mW and a signal sweeping power range of 0.48–4.8 mW. The result is shown in the inset of Fig. 7(a), where the linear fit (dashed line) agrees well with the relation $P_{\mathrm{DF}} \propto P_pP_s$. The slope of the linear fit in the graph of P_{DF} versus P_pP_s provides an estimation of the DFG conversion efficiency defined as $\eta = P_{\mathrm{DF}}/(P_pP_s)$. For the characterized device, η was found to be $\approx 5.7 \times 10^{-4}$ $\%\mathrm{W}^{-1}$. This efficiency is equal to 2.5×10^{-2} $\%\mathrm{W}^{-1} \cdot \mathrm{cm}^{-2}$ when normalized to the device length. It should be noted that the DFG efficiency reported here is the external value. The internal efficiency, which requires the estimation of the internal powers inside the device, is considerably larger than the external one. The internal pump power could not be determined due to difficulties in extracting the linear coupling factor defined as the spatial overlap between the incident pump beam and the excited pump, which is a Bragg mode. Simulations indicate that this coupling efficiency is likely to be a few percent, which implies that a low pump power level is likely to be responsible for the output powers measured. Several routes can be undertaken to further enhance the DFG process in BRWs. These include preferential coupling to Bragg mode by using prism coupling, grating-assisted coupling, or by using spatial light modulators. In a more advanced scheme, these coupling techniques can be completely avoided by developing self-pump DFG devices, where a Bragg laser pump [51] with phase-matched cavity is fabricated on the same wafer platform.

A typical spectrum taken at the waveguide output is shown in Fig. 7(b). The pump was set at 777.8 nm with a signal at 1545.9 nm. The DF wavelength was observed at 1565.4 nm. From the spectra, the power level of DF was -62.5 dB lower

than that of the signal. The spectra in Fig. 7(b) denotes an additional spectral feature at $\approx 2\lambda_p = 1555.6$ nm, which is due to the second-order diffraction of the pump from the grating of the optical spectrum analyzer. This was confirmed by the fact that the spectral feature at 1555.6 nm remained unchanged, while the DF spectra shifted in the opposite direction to the signal during tuning.

The inset of Fig. 7(b) shows the DFG tuning curve, which was obtained by detuning the pump wavelength from degeneracy while tracking the wavelengths of signal and DF for maximal DF power. It was observed that a detuning of the pump wavelength by 0.4 nm resulted in a span of ≈40 nm between signal and DF wavelengths. Further detuning of the pump from degeneracy was expected to offer broader separation between signal and DF. This could not be confirmed experimentally due to the aforementioned constraints in tuning the signal wavelength.

D. Bandgap Effect for High Pump Power Operation

The $\mathrm{BRW_I}$ device demonstrated notable efficiency enhancement afforded by improving the nonlinear overlap factor ξ in an SHG process. The structure of $\mathrm{BRW_I}$ incorporated $\mathrm{Al}_x\mathrm{Ga}_{1-x}\mathrm{As}$ layers with aluminum concentrations as low as $x = 0.20$ with an associated bandgap of ≈1.67 eV. This ensures that the pump is below half the bandgap of the layers constituents in a structure used for SHG experiments. This will, in turn, serve to minimize the effects of third-order nonlinearities, which would improve the device performance. However, as the material bandgap detunes further away from the operating wavelength, the effective nonlinearity is reduced. To highlight the effects of this tradeoff, it is instructive to examine the conversion efficiency with pump power. The structure studied here shows that the efficiency of SHG in $\mathrm{BRW_I}$ was restrained to internal pump average powers below ≈9 mW. For pump powers above 9 mW, saturation of second-harmonic power was clearly observed, which was understood as a result of degrading effects of $\chi^{(3)}$ nonlinearities, such as 2PA and self-phase modulation (SPM).

To illustrate this, we examine the dependency of second-harmonic power on the pump power obtained by using three different pulsed laser systems, namely, 1) a programmable laser from Genia Photonics Inc. [53] generating pulses with 30-ps temporal width ($\Delta\tau$) at a repetition rate (f_{rep}) of 15 MHz; 2) an OPO synchronously pumped by a mode-locked Ti:Sapphire laser generating 2-ps pulses at 76-MHz repetition rate; and 3) the same OPO system converted to 250-fs pulses at 76-MHz repetition rate. Characterizing the device under different pulsed-pump conditions would provide a better insight into the nonlinear interaction, particularly at high pump power levels. Fig. 8 depicts the variation of SH power as a function of pump wavelength obtained by using the three laser sources. From the figure, it can be seen that when using 30- and 2-ps pulses, P_{SH} saturates around the pump average power of 9 mW to a value of approximately $P_{\mathrm{SH}} = 300\ \mu$W. For pump powers above ≈9 mW, the generated SH power fails to follow the quadratic relation of $P_{\mathrm{SH}} \propto P_p^2$ as a result of $\chi^{(3)}$ nonlinearities.

It is well known that the third-order effects are more pronounced for low-aluminum-concentration $\mathrm{Al}_x\mathrm{Ga}_{1-x}\mathrm{As}$ elements due to smaller bandgaps [63], [64]. In order to overcome the saturation of generated harmonics at high pump powers, we

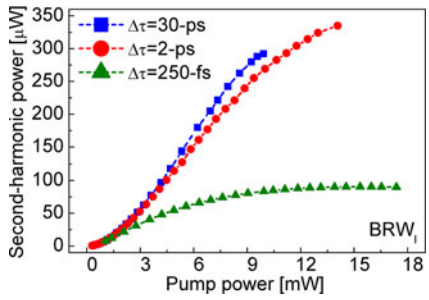

Fig. 8. Dependency of generated SH power on pump power in $\mathrm{BRW_I}$ waveguide characterized using 30-ps, 2-ps, and 250-fs pulsed pump.

aimed at redesigning ML-BRW devices with high-aluminum-content $\mathrm{Al}_x\mathrm{Ga}_{1-x}\mathrm{As}$ elements. However; simulations show that using elements with high aluminum concentrations in ML-BRWs compromise the nonlinear overlap factor and the structure's effective second-order nonlinear coefficient, hence reducing the efficiency of the nonlinear interaction. The reduction of the nonlinear overlap factor, when high-aluminum-fraction elements are incorporated, is qualitatively addressed by the fact that the material index contrast between the layers as well as the material dispersion are reduced with the increase of the aluminum content of $\mathrm{Al}_x\mathrm{Ga}_{1-x}\mathrm{As}$ layers. The low index contrast between the layers along with the reduced material dispersion gives rise to weakly confined optical modes with a degraded spatial overlap factor. In addition, the reduction of the structure's effective nonlinear coefficient due to the increase of aluminum concentrations is apparent, as the d_{eff} of individual $\mathrm{Al}_x\mathrm{Ga}_{1-x}\mathrm{As}$ elements also reduces with the increase of aluminum fraction [56].

This tradeoff of the reduction of nonlinear overlap factor and the structure's effective nonlinearity in devices, which incorporate elements with high aluminum concentration can be addressed by a simple extension to ML-BRW designs, referred to as multilayer-core ML-BRWs. In the proposed design, the waveguide core is a multilayer dielectric structure. Engineering individual layers of the multilayer core in the proposed design is expected to be greatly effective in modifying modal behaviors, as the optical fields within the core layers are the strongest. As discussed in the following section, in a multilayer-core ML-BRW, the characteristics of the core layers, including their indexes and thicknesses, offer additional design parameters that can be exploited for improving the spatial overlap factor and the effective nonlinear coefficient of the design, thereby enhancing the nonlinear conversion efficiency.

IV. Multilayer-Core ML-BRWs

We start by developing the analytical tools required for designing multilayer-core ML-BRWs. Our approach for deriving the modal dispersion equations and the ML thickness rely on applying the boundary conditions of field transitions at the interface between the ML and quarter-wave Bragg reflector. We consider two general designs, namely, a symmetric ML-BRW, where the structure possesses geometrical symmetry with respect to the core center and a mono-stack ML-BRW, where one of the periodic claddings in a symmetric structure is replaced by a single layer or by a periodic dielectric layers. The schematic of a multilayer-core symmetric ML-BRW is shown in Fig. 9(a).

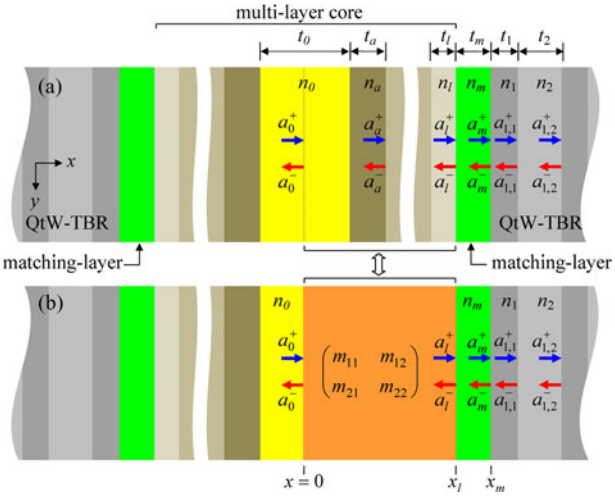

Fig. 9. (a) Schematic of a multilayer-core symmetric ML-BRW. The ML separates the multilayer core composed of dielectric layers with the refractive indexes $n_0, n_a, n_b, \ldots, n_l$ from the quarter-wave Bragg reflectors. (b) Conceptual structure, where half of the core center layer with index n_0 and $n_a, n_b, \ldots, n_l$ layers in (a) are represented by an $ABCD$ matrix with elements $m_{11}, \ldots, m_{22}$.

In this structure, the core is composed of multiple dielectric layers with refractive indexes $n_0, n_a, n_b, \ldots, n_l$ and associated thicknesses $t_0, t_a, t_b, \ldots, t_l$. The ML with a refractive index of n_m and a thickness of t_m separates the multilayer core from the quarter-wave Bragg reflector. We assume that the Bragg reflectors are composed of bilayers with refractive indexes n_1 and n_2 with associated thicknesses of t_1 and t_2. To design the structure, it is assumed that all material indexes are given *a priori*. Also, the thicknesses of the dielectric layers composing the complex core, $t_a, t_b, \ldots, t_l$, are assumed to be given. The thickness of the ML is then used for tailoring the effective-mode index of the structure such that the bilayers of the Bragg reflectors satisfy the quarter-wave condition of

$$k_1^x t_1 = (2u+1)\frac{\pi}{2} \qquad k_2^x t_2 = (2v+1)\frac{\pi}{2} \tag{7}$$

where $u, v = 0, 1, 2, \ldots$, and k_1^x and k_2^x are the x-components of the wave vectors in the bilayers of the Bragg mirrors.

The modal dispersion equations and the required ML thickness of the multilayer-core symmetric ML-BRW can be obtained by applying the boundary condition of transition of overall electric field amplitude at the interface between the ML and QtW-TBR. The overall field amplitude, formed by the superposition of the right- and left-propagating plane waves, either vanishes or peaks at the interface between the QtW-TBR and the ML, the immediate layer before the TBR. Referring to Fig. 9, this condition requires that $a_m^+ + a_m^- = 0$ or $a_m^+ - a_m^- = 0$ in order to obtain a node or antinode at $x = x_m$, respectively. The extraction of the modal dispersion equation and ML thickness requires multiplication of the propagation matrix for a propagation of $t_0/2$ and the transfer matrixes of layers $n_a, n_b, \ldots, n_l$, and subsequently solving for t_m. Although theoretically feasible, one can find this approach mathematically tedious, which requires different solutions for different numbers of complex core layers. Here, a generic solution is proposed, which can be utilized for any given number of core layers.

We start by relating the right- and left-propagating field amplitudes of the core (a_0^+, a_0^-) to those of the layer prior to the ML (a_l^+, a_l^-). This relation is expressed as

$$\begin{bmatrix} a_l^+ \\ a_l^- \end{bmatrix} = \mathbf{M} \begin{bmatrix} a_0^+ \\ a_0^- \end{bmatrix} = \begin{bmatrix} m_{11} & m_{12} \\ m_{21} & m_{22} \end{bmatrix} \begin{bmatrix} a_0^+ \\ a_0^- \end{bmatrix} \tag{8}$$

where the matrix $\mathbf{M}$ with elements $m_{11}, \ldots, m_{22}$ is an $ABCD$ matrix, which replaces half of the core center layer with index/thickness of n_0/t_0 and the layers $n_a, n_b, \ldots, n_l$, as shown in Fig. 9(b). Here, we are interested in the lowest order even Bragg mode, for which the superposition of right- and left-propagating fields within the core is maximum. Due to the symmetry of the structure, one can assume that $a_0^+ = a_0^-$. Without loss of generality, the overall field amplitude at the core center is taken to be unity such that $a_0^+ = a_0^- = 1/2$. Using transfer matrices of the core layers $n_a, n_b, \ldots, n_l$, the field amplitudes in the layer before the ML, the lth layer, are expressed as

$$a_l^+ = \frac{(m_{11} + m_{12})}{2} \qquad a_l^- = \frac{(m_{21} + m_{22})}{2}. \tag{9}$$

Given a_l^+ and a_l^-, the field amplitudes in the ML can be calculated using the single transfer matrix as

$$\begin{bmatrix} a_m^+ \\ a_m^- \end{bmatrix} = \mathbf{T}_m \begin{bmatrix} a_l^+ \\ a_l^- \end{bmatrix}. \tag{10}$$

In (10), $\mathbf{T}_m$ is the forward transfer matrix of the ML, which is defined as

$$\mathbf{T}_m = \frac{1}{2}\begin{bmatrix} (1+f_P)\exp(-i\phi_m) & (1-f_P)\exp(-i\phi_m) \\ (1-f_P)\exp(+i\phi_m) & (1+f_P)\exp(+i\phi_m) \end{bmatrix} \tag{11}$$

where $P = \{\mathrm{TE}, \mathrm{TM}\}$ is the subscript used for indicating the polarization state of the propagating field, $\phi_m = k_m^x t_m$ is the phase accumulated in the ML and

$$f_P = \begin{cases} \dfrac{k_l^x}{k_m^x}, & \text{for TE polarization} \\ \dfrac{n_m^2 k_l^x}{n_l^2 k_m^x}, & \text{for TM polarization.} \end{cases} \tag{12}$$

Using (10), the ML field amplitudes are derived as

$$a_m^+ = \frac{1}{4}[(m_{11} + m_{12})(1+f_P)\exp(-i\phi_m) + (m_{21} + m_{22})(1-f_P)\exp(-i\phi_m)] \tag{13a}$$

$$a_m^- = \frac{1}{4}[(m_{11} + m_{12})(1-f_P)\exp(+i\phi_m) + (m_{21} + m_{22})(1+f_P)\exp(+i\phi_m)]. \tag{13b}$$

For TE propagating mode, the electric field vanishes ($a_m^+ + a_m^- = 0$) at $x = x_m$ for $k_m^x < k_1^x$ and it peaks ($a_m^+ - a_m^- = 0$) for $k_m^x > k_1^x$. Using (13a) and (13b), the modal dispersion for TE mode is obtained as

$$\begin{aligned} \cot(k_m^x t_m) &= +i f_{\mathrm{TE}}\zeta, \ (k_m^x < k_1^x) \\ \tan(k_m^x t_m) &= -i f_{\mathrm{TE}}\zeta, \ (k_m^x > k_1^x) \end{aligned} \tag{14}$$

where ζ is a complex number defined as

$$\zeta = \frac{m_{11} + m_{12} - m_{21} - m_{22}}{m_{11} + m_{12} + m_{21} + m_{22}}. \tag{15}$$

Equations (14) can be solved to calculate the thickness of the ML as

$$t_m = \frac{1}{k_m^x}\left[\text{acot}\left(+if_{\text{TE}}\zeta\right)+p\pi\right], (k_m^x < k_1^x)$$
$$t_m = \frac{1}{k_m^x}\left[\text{atan}\left(-if_{\text{TE}}\zeta\right)+p\pi\right], (k_m^x > k_1^x) \quad (16)$$

where $p = 0, 1, 2, \ldots$ is the ML thickness scaling factor.

For TM propagation, the electric field vanishes at $x = x_m$ for $n_1^2 k_m^x < n_m^2 k_1^x$, and it peaks for $n_1^2 k_m^x > n_m^2 k_1^x$. Using (13a) and (13b), modal dispersion of TM propagating mode is obtained as

$$\cot(k_m^x t_m) = +if_{\text{TM}}\zeta, \quad (n_1^2 k_m^x < n_m^2 k_1^x)$$
$$\tan(k_m^x t_m) = -if_{\text{TM}}\zeta, \quad (n_1^2 k_m^x > n_m^2 k_1^x). \quad (17)$$

Solving (17) for t_m, the thickness of the ML is given as

$$t_m = \frac{1}{k_m^x}\left[\text{acot}\left(+if_{\text{TM}}\zeta\right)+p\pi\right], (n_1^2 k_m^x < n_m^2 k_1^x)$$
$$t_m = \frac{1}{k_m^x}\left[\text{atan}\left(-if_{\text{TM}}\zeta\right)+p\pi\right], (n_1^2 k_m^x > n_m^2 k_1^x). \quad (18)$$

For the case that the structure is composed of lossless dielectrics, the aforementioned equations can be further simplified. In order to show this, it is useful to recall that when the waveguide layers are lossless, the elements of the matrix $\mathbf{M}$ in (8) inherit the property that $m_{22} = m_{11}^*$ and $m_{21} = m_{12}^*$. Defining the complex number ζ as

$$\zeta = |\zeta|\exp(i\phi_\zeta) = m_{11} + m_{12} \quad (19a)$$
$$\tan\phi_\zeta = \frac{\text{Im}[\zeta]}{\text{Re}[\zeta]} = \frac{\text{Im}[m_{11}+m_{12}]}{\text{Re}[m_{11}+m_{12}]}. \quad (19b)$$

For TE polarization, (14) can then be simplified as

$$\cot(k_m^x t_m) = +if_{\text{TE}}\tan\phi_\zeta, (k_m^x < k_1^x)$$
$$\tan(k_m^x t_m) = -if_{\text{TE}}\tan\phi_\zeta, (k_m^x > k_1^x) \quad (20)$$

with the ML thickness expressed as

$$t_m = \frac{1}{k_m^x}\left[\text{acot}\left(-f_{\text{TE}}\tan\phi_\zeta\right)+p\pi\right], \quad (k_m^x < k_1^x)$$
$$t_m = \frac{1}{k_m^x}\left[\text{atan}\left(+f_{\text{TE}}\tan\phi_\zeta\right)+p\pi\right], \quad (k_m^x > k_1^x). \quad (21)$$

Similarly, for TM propagation, (17) can be simplified as

$$\cot(k_m^x t_m) = +if_{\text{TM}}\tan\phi_\zeta, (n_1^2 k_m^x < n_m^2 k_1^x)$$
$$\tan(k_m^x t_m) = -if_{\text{TM}}\tan\phi_\zeta, (n_1^2 k_m^x > n_m^2 k_1^x) \quad (22)$$

with the ML thickness given by

$$t_m = \frac{1}{k_m^x}\left[\text{acot}\left(-f_{\text{TM}}\tan\phi_\zeta\right)+p\pi\right], (n_1^2 k_m^x < n_m^2 k_1^x)$$
$$t_m = \frac{1}{k_m^x}\left[\text{atan}\left(+f_{\text{TM}}\tan\phi_\zeta\right)+p\pi\right], (n_1^2 k_m^x > n_m^2 k_1^x). \quad (23)$$

Equations (14)–(18) serve as the design equations for multilayer-core symmetric ML-BRWs. The physical parameters of the complex core layers, including their refractive indexes and thicknesses, offer extra degrees of freedom for design optimization. Although in our analysis we assumed that the phases in each of the core layers do not establish any particular relations with each other, in practice, we can impose particular phase relations among them. For example, one can design a double grating mirror, where the layers $n_a, n_b, \ldots, n_l$ form a periodic structure with quarter-wave bilayers with high reflectivity at a given wavelength of λ_1, while the TBRs are designed to have high reflection at a different wavelength of λ_2. The ML then operates as a phase tuning layer between the two high-reflection periodic structures.

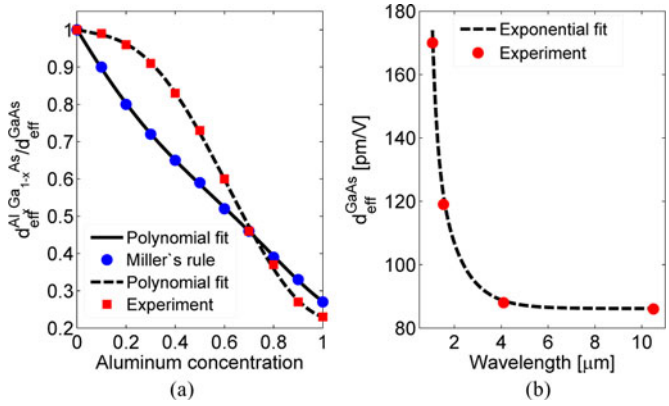

Fig. 10. (a) Dependency of $d_{\text{eff}}^{\text{Al}_x\text{Ga}_{1-x}\text{As}}/d_{\text{eff}}^{\text{GaAs}}$ on aluminum molar concentration extracted using the data reported in [56]. The solid line and the dashed line show the fifth-order polynomial fits used to obtain a numerical model for estimating the effective nonlinearity. (b) Variation of $d_{\text{eff}}^{\text{GaAs}}$ as a function of wavelength obtained by using the reported experimental data in [57] (filed circle) and an extracted exponential decay fit (dashed line).

V. Device Design and Performance

A. Extracted Model for d_{eff} of Bulk $Al_xGa_{1-x}As$

Theoretical calculations of nonlinear conversion efficiency requires an approximation for the waveguide d_{eff}. While the values of d_{eff} for bulk $\text{Al}_x\text{Ga}_{1-x}\text{As}$ can be theoretically estimated by using Miller's rule [55], the literature lacks a comprehensive model, which provides the dependency of d_{eff} as a function of aluminum concentration, operation wavelength, and temperature. Ohashi *et al.* [56] reported the experimentally measured dependence of the ratio $d_{\text{eff}}^{\text{Al}_x\text{Ga}_{1-x}\text{As}}/d_{\text{eff}}^{\text{GaAs}}$ as a function of Al concentration obtained by using Nd:YAG laser that operates at 1064 nm. Here, we adopt the reported data in [56] to extract a numerical model for estimating d_{eff} of bulk $\text{Al}_x\text{Ga}_{1-x}\text{As}$. Fig. 10(a) illustrates the extracted data of $d_{\text{eff}}^{\text{Al}_x\text{Ga}_{1-x}\text{As}}/d_{\text{eff}}^{\text{GaAs}}$ from [56] along with the fifth-order polynomial fit

$$\frac{d_{\text{eff}}^{\text{Al}_x\text{Ga}_{1-x}\text{As}}}{d_{\text{eff}}^{\text{GaAs}}} = \sum_{m=0}^{5} c_m x^m \quad (24)$$

which we used as the theoretical models for the ratio of $d_{\text{eff}}^{\text{Al}_x\text{Ga}_{1-x}\text{As}}/d_{\text{eff}}^{\text{GaAs}}$. The coefficients of the polynomial fits for each graph in Fig. 10(a) are summarized in Table II.

Equation (24) requires a numerical value for $d_{\text{eff}}^{\text{GaAs}}$. Although the fits in Fig. 10(a) were obtained for the wavelength of

TABLE II
COEFFICIENTS OF FIFTH-ORDER POLYNOMIAL IN (25)

Coefficient	Miller's rule	Experimental value
c_0	1.000	1.000
c_1	-1.077	-0.176
c_2	0.202	0.870
c_3	1.661	-6.011
c_4	-2.797	6.469
c_5	1.282	-1.923

TABLE III
CONSTANTS OF THE EXPONENTIAL DECAY FIT USED FOR MODELING THE DEPENDENCY OF $d_{\text{eff}}^{\text{GaAs}}$ ON WAVELENGTH OBTAINED BY USING THE REPORTED DATA IN [57]

d_0 [pm/V]	d_1 [pm/V]	λ_1 [nm]	d_2 [pm/V]	λ_2 [nm]	d_3 [pm/V]	λ_3 [nm]
86	4058	194	4081	194	152	993

1064 nm, we assumed that the slopes of the fits more or less follows the same trends at other wavelengths. In order to use (24), one needs a numeric for the value of $d_{\text{eff}}^{\text{GaAs}}$ at a given wavelength. In our model, we estimated $d_{\text{eff}}^{\text{GaAs}}$ by using the discrete values reported in [57]. Using a shape-preserving interpolation fit followed by an exponential decay fit, as illustrated in Fig. 10, we derived an extracted model for the values of $d_{\text{eff}}^{\text{GaAs}}$ reported in [57] as

$$d_{\text{eff}}^{\text{GaAs}}(\lambda) = d_0 + d_1 \exp\left(-\frac{\lambda}{\lambda_1}\right) + d_2 \exp\left(-\frac{\lambda}{\lambda_2}\right) + d_3 \exp\left(-\frac{\lambda}{\lambda_3}\right) \quad (25)$$

where $d_0, \ldots, d_3$ and $\lambda_1, \ldots, \lambda_3$ are the fitting constants, which are given in Table III.

Using the above discussed model of d_{eff} for bulk $\text{Al}_x\text{Ga}_{1-x}\text{As}$ elements, an estimation for the effective nonlinear coefficient of the BRW structures could be obtained by applying (5).

B. Device Description and Characterization

The multilayer-core ML-BRW design, discussed in the previous section, offers additional flexibility in the choice of materials for phase-matched structures. Using this technique, we designed a new wafer, referred to as BRW_{II}, which utilized materials with high aluminum concentration $\text{Al}_x\text{Ga}_{1-x}\text{As}$, while constraining the minimum Al concentration within the structure to $x = 0.35$ with a bandgap of ≈1.87 eV. The choice of $\text{Al}_x\text{Ga}_{1-x}\text{As}$ elements with $x > 0.35$ introduced the tradeoff of reducing the nonlinear conversion efficiency η, since both the effective nonlinear coefficient of the structure and the nonlinear overlap factor were reduced. However, the multilayer-core ML-BRW design made it possible to mostly compensate for the reduction of nonlinear conversion efficiency while incorporating high aluminum concentration layers. Here, we discuss the benefits offered by BRW_{II} device in comparison to BRW_{I}, particularly when high pump power operation is desired.

The epitaxial structure of BRW_{II} wafer is shown in Fig. 11, where the waveguide multilayer core and the QtW-TBRs are separated by the ML. In designing BRW_{II}, the optimization objective function was taken as $\bar{\eta}_{\text{SHG}}$ for type-II process, taking into consideration the influence of both ξ and the structure d_{eff}. This was in contrast to the design of BRW_{I}, where the

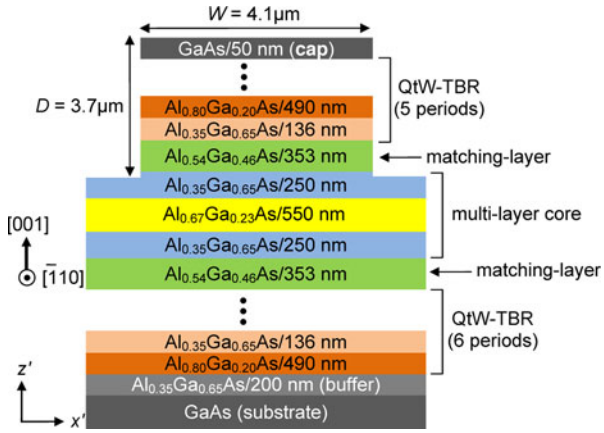

Fig. 11. Epitaxial structure of the BRW_{II} device. The top/bottom QtW-TBRs are separated from the three-layer core by the ML.

TABLE IV
SIMULATED NONLINEAR PARAMETERS OF SLAB BRW_{I} AND BRW_{II} DESIGNS FOR TYPE-II SHG

Design	λ_p [nm]	ξ $[\text{m}]^{-1}$	d_{eff} [pm/V]	$\bar{\eta}_{\text{SHG}}$ $[\%\text{W}^{-1}\text{cm}^{-2}]$
BRW_{I}	1546.5	221	40	3.0×10^{-4}
BRW_{II}	1540.0	133	38	1.1×10^{-4}

nonlinear overlap factor was regarded as the primary optimization objective function. Simulated nonlinear properties of both devices is summarized in Table IV. From this table, it can be seen that while BRW_{II} incorporated materials with high aluminum fractions, its conversion efficiency is within the same order of magnitude as that of BRW_{I}. Using the table, the efficiency of BRW_{II} was expected to be approximately one-third of the efficiency of BRW_{I}, provided that propagation losses in the two devices were comparable. The theoretical estimations of $\bar{\eta}_{\text{SHG}}$ in Table IV does not take into account $\boldsymbol{\chi}^{(3)}$ nonlinear effects when a high pump power is employed. As will be discussed, BRW_{II} was indeed a superior design in comparison to BRW_{I} under high pump condition due to the employment of $\text{Al}_x\text{Ga}_{1-x}\text{As}$ layers with higher aluminum contents with larger bandgaps.

The wafer of BRW_{II} was grown on $[0\,0\,1]$ GaAs substrate using MOCVD. Using plasma etching, ridge structures were patterned on typical sample. Characterizations were carried out on a ridge waveguide which had a width of 4.1μm and a depth of 3.7 μm. The length of the device was 1.7 mm. Using the Fabry–Pérot technique, linear propagation losses of TE- and TM-polarized pump mode around 1550 nm were determined to be 2.2 and 2.9 cm^{-1}, respectively. The input coupling factor and facet reflectivity were estimated to be 0.48 and 0.29, respectively.

Similar to the characterization of BRW_{I}, we evaluated the performance of BRW_{II} sample for SHG by using the 30-ps, 2-ps, and 250-fs pulsed-pump lasers. Table V provides a summary of the examined SHG parameters of both devices, including PM wavelength (λ_{PM}), FWHM pump spectral bandwidth ($\Delta\lambda_p$), FWHM second-harmonic spectral bandwidth ($\Delta\lambda_{\text{SH}}$), internal SH average power (P_{SH}), wavelength acceptance bandwidth (FWHM) of SHG tuning curve ($\Delta\lambda_{\text{SHG}}$), normalized nonlinear conversion efficiency ($\bar{\eta}_{\text{SHG}}$), and the ratio

TABLE V
SUMMARY OF SHG CHARACTERIZATION AT $P_p = 2.2$ mW

Parameter	BRW_I	BRW_{II}	BRW_I	BRW_{II}	BRW_I	BRW_{II}
$\Delta\tau$ [ps]	30	30	2	2	0.25	0.25
f_{rep} [MHz]	15	15	76	76	76	76
$\Delta\lambda_p$ [nm]	0.3	0.3	2.5	2.5	75	75
$\Delta\lambda_{SH}$ [nm]	0.27	0.25	0.38	0.48	1.2	1.3
P_{SH} [μW]	32.8	6.6	32.0	4.7	11.2	1.6
λ_{PM} [nm]	1554.0	1559.6	1553.4	1558.9	1560.1	1556.2
$\bar{\eta}_{SHG}$ [$\%W^{-1}cm^{-2}$]	1.4×10^4	4.6×10^3	1.4×10^4	3.2×10^3	4.8×10^3	1.1×10^3
$\bar{\eta}_{SHG,CW}$ [$\%W^{-1}cm^{-2}$]	6.30	2.07	2.13	0.49	0.09	0.02
$\Delta\lambda_{SHG}$ [nm]	0.6	1.0	1.9	2.7	36	38
$\Delta\lambda$	2.0	3.3	0.8	1.1	0.5	0.5

$\Delta\lambda = \Delta\lambda_{SHG}/\Delta\lambda_p$. Also included in Table V is the equivalent CW conversion efficiency $\bar{\eta}_{SHG,CW}$, which was calculated by multiplying $\bar{\eta}_{SHG}$ with the pulse duty cycle $\Delta\tau f_{rep}$. The numeric of $\bar{\eta}_{SHG,CW}$ provided a merit of the device efficiency independent of the pulse temporal width and repetition rate. All parameters in the table were obtained for a pump with an internal average power of $P_p = 2.2$ mW.

Representative interpretation of the data in Table V requires the pump peak power, pump spectral width, and third-order nonlinear effects to be taken into consideration. From the table, it can be seen that for either device, changing the pulse width from 30 to 2 ps did not significantly affect the generated SH power and the conversion efficiency. Although the temporal pulsewidths of 30- and 2-ps laser systems were different by over an order of magnitude, the duty cycle of the pulses were within the same order of magnitude. For the 30-ps laser, the pulse duty cycle was 4.5×10^{-4}, while it was 1.5×10^{-4} for the 2-ps laser. Assuming nearly-transform-limited pulses, when pump power is fixed, it can be deduced that the peak powers in 30- and 2-ps systems were within the same order of magnitude. Hence, the generated SH should be comparable. On the other hand, pulses in 250-fs system had a duty cycle of 1.9×10^{-5}, which was approximately an order of magnitude less than those in the other two laser systems. The smaller duty cycle of the femtosecond pulses translated to approximately an order of magnitude enhancement in the pump peak power. However, from Table V, the generated SH power and the nonlinear conversion efficiency in the 250-fs system were considerably reduced with respect to those obtained using longer pulsewidths.

A comparison between the pump spectral bandwidth $\Delta\lambda_p$ and the wavelength acceptance bandwidth (FWHM) of SHG tuning curve $\Delta\lambda_{SHG}$, measured in these three laser systems, can partly explain the lower efficiency in femtosecond SHG. To show this, we consider the ratio $\Delta\lambda = \Delta\lambda_{SHG}/\Delta\lambda_p$ as a figure of merit that indicates the portion of the pump spectra utilized in the SHG. Using Table V, for 30-ps pulses, the entire pump spectra is utilized in both devices. For BRW_{II}, $\Delta\lambda = 2.0$, while for BRW_I, $\Delta\lambda = 3.3$. On the other hand, for 250-fs pulses, $\Delta\lambda = 0.5$, which denotes that approximately half of the pump spectra was utilized for SHG in both devices. In using ultrashort pulses, particularly in the femtosecond regime, other factors contribute to reduce the generated harmonic power and the efficiency of the interaction. These factors include dispersion effects, such as group velocity mismatch and group velocity dispersion, as well as the degrading effects of third-order nonlinearities [65].

In order to verify the effect of stronger dispersion in reducing the efficiency of SHG in femtosecond pulse regime, it would

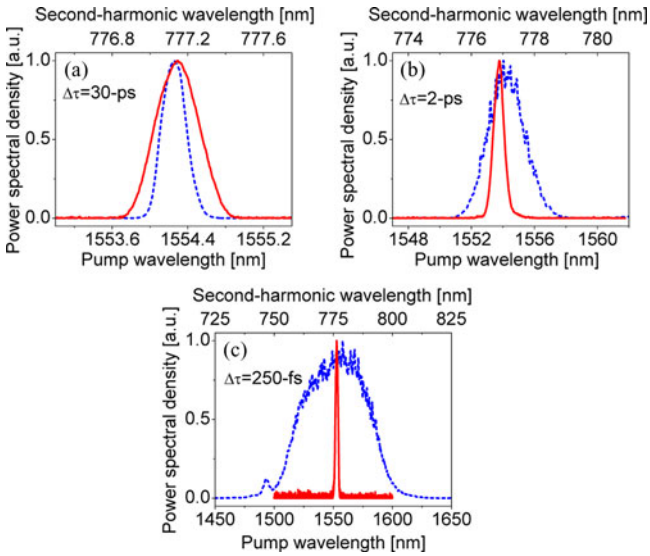

Fig. 12. Power spectral densities of the pump (dashed line) and second harmonic (solid line) in BRW_I waveguide measured using (a) 30-ps, (b) 2-ps, and (c) 250-fs pulses. The FWHM spectral bandwidth of the pump λ_p and that of the SH λ_{SH} for each pulsed system is given in Table V.

be informative to examine the spectral bandwidth of the generated second-harmonic signal. From theory, the power of the SH signal and that of the pump follows the well-known relation of $P_{SH} \propto P_p^2 \text{sinc}^2(\Delta\beta L/2)$, where $\Delta\beta = 2\beta_p - \beta_{SH}$ is the wavenumber mismatch between the propagation constants of the pump β_p and the second-harmonic β_{SH}. As such, the spectral bandwidth of the generated SH signal depends on the pump spectral function as well as the phase-mismatch term. In comparison to picosecond operation, femtosecond pulses exhibit larger modal dispersion results in increasing $\Delta\beta$, hence decreasing the width of the function $\text{sinc}^2(\Delta\beta L/2)$. To illustrate this, in Figs. 12 and 13, we have plotted the normalized powers spectral densities of the pump and the second harmonic for BRW_I and BRW_{II} devices, respectively, obtained BY using 30-ps, 2-ps, and 250-fs pulses. Table V contains the measured values of the spectral bandwidths of the pump $\Delta\lambda_p$ and the second harmonic $\Delta\lambda_{SH}$. From the figures, it can be observed that, for either device, the ratio of second-harmonic spectral bandwidth to that of the pump $\Delta\lambda_{SH}/\Delta\lambda_p$ is the lowest in using 250-fs pulses. For example, for BRW_I sample in Fig. 12 and using Table V, for 30-ps pulses, $\Delta\lambda_{SH}/\Delta\lambda_p = 0.9$, while for 250-fs pulses, $\Delta\lambda_{SH}/\Delta\lambda_p = 0.02$. The small ratio of $\Delta\lambda_{SH}/\Delta\lambda_p$ in

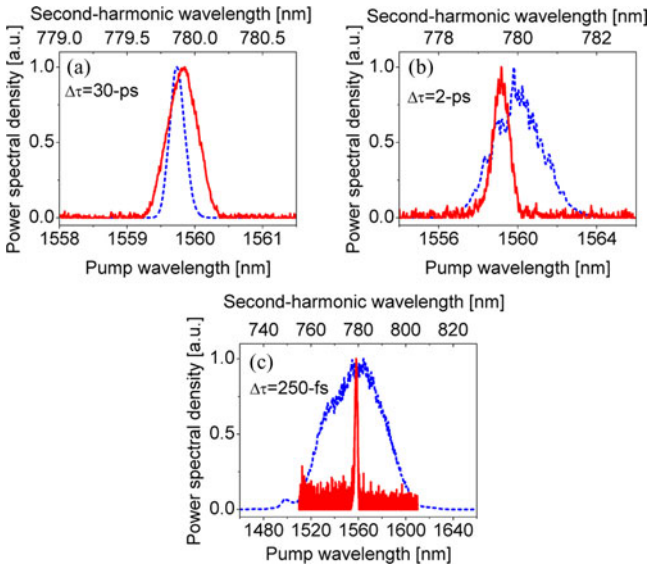

Fig. 13. Power spectral densities of the pump (dashed line) and second harmonic (solid line) in BRW_{II} waveguide measured by using (a) 30-ps, (b) 2-ps, and (c) 250-fs pulses. The FWHM spectral bandwidth of the pump λ_p and that of the SH λ_{SH} for each pulsed system is given in Table V.

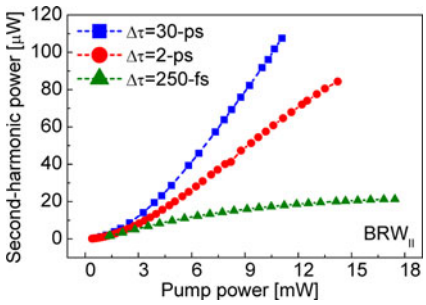

Fig. 14. Dependency of generated SH power on pump power in BRW_{II} waveguide characterized by using 30-ps, 2-ps, and 250-fs pulsed pump.

femtosecond regime is a clear indication of the reduction of SHG efficiency due to enhanced modal dispersion.

In Fig. 14, we have illustrated the variation of P_{SH} as a function of pump power obtained by using the three pulsed-laser systems for BRW_{II}. Comparing Figs. 8 and 14 denotes that both devices show the maximum increase of P_{SH} when using 30-ps pulses. In contrast, from Fig. 14 for 30-ps pulses, the quadratic relation between P_{SH} and P_p is mostly maintained over the entire sweeping range of P_p for BRW_{II}. This clearly suggests that the generated second-harmonic power in BRW_{II} could be further enhanced by increasing the device length.

To further distinguish the operation of both samples under high pump power conditions, we normalized the generated SH power in each device by the square of the sample length to obtain a figure of merit for harmonic generation independent of the device length. This normalization was supported by the fact that the measured losses in the two samples were comparable. Fig. 15(a) illustrates the variation of P_{SH}/L^2 as functions of pump powers when using 30-ps pulses. In the figure, the dotted-lines are the theoretical quadratic fits of $P_{SH} \propto P_p^2$. The rollover of P_{SH} in BRW_I sample, as can be observed in Fig. 15(a), is

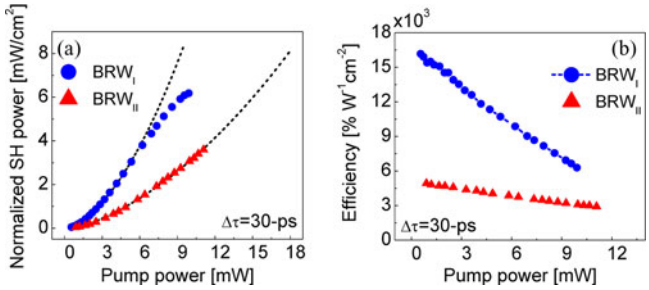

Fig. 15. (a) Second-harmonic power normalized to square of device length as a function of internal pump power obtained by using 30-ps pulses. The dotted lines are theoretical quadratic fits. (b) Normalized SHG conversion efficiency estimated in using 30-ps pulsed pump.

a clear indication of the superior performance of BRW_{II} when high pump power is employed.

Finally in Fig. 15(b), we have plotted the normalized conversion efficiencies of the characterized devices. Both samples show that their efficiencies decreased with the increase of pump power. For BRW_I, the decay rate of $\bar{\eta}_{SHG}$ was considerably greater in comparison to BRW_{II}, which was ascribed to stronger $\chi^{(3)}$ effects.

VI. Conclusion

In summary, we reviewed the recent advances for PM SHG, SFG, and DFG by using ML-BRW. Although ML-BRW design was demonstrated as an efficient PM technique at low pump powers, power saturation of the generated harmonic at high pump power was observed due to the limitations posed by third-order nonlinearities for the choice of waveguide layer constituents. The multilayer-core ML-BRW design was proposed and demonstrated as a possible design route for relaxing the constraints over the choice of materials in phase-matched BRWs. The multilayer-core ML-BRWs are expected to aid realization and enhance the efficiency of photonic devices, such as electrically pumped integrated optical parametric oscillators, where high pump power is essential.

Acknowledgment

The authors would like to thank J. S. Aitchison for the 2-ps characterization setup, Genia Photonics Inc. for the 30-ps pulsed fiber laser, and CMC Microsystems for growing the wafers.

References

[1] P. A. Franken, G. Weinreich, C. W. Peters, and A. E. Hill, "Generation of optical harmonics," *Phys. Rev. Lett.*, vol. 7, no. 4, pp. 118–119, Aug. 1961.

[2] J. A. Armstrong, N. Bloembergen, J. Ducuing, and P. S. Pershan, "Interactions between light waves in a nonlinear dielectric," *Phys. Rev.*, vol. 127, no. 6, pp. 1918–1939, Sep. 1962.

[3] M. M. Fejer, G. A. Magel, D. H. Jundt, and R. L. Bye0r, "Quasi-phasematched second harmonic generation: Tuning and tolerances," *IEEE J. Quantum Electron.*, vol. 28, no. 11, pp. 2631–2654, Nov. 1992.

[4] Y. S. Liu, D. Dentz, and R. Belt, "High-average-power intracavity second-harmonic generation using $KTiOPO_4$ in an acousto-optically Q-switched Nd-YAG laser-oscillator at 5 KHz," *Opt. Lett.*, vol. 9, no. 3, pp. 76–78, Mar. 1984.

[5] K. Kato, "Second-harmonic generation to 2048 Åin β-BaB_2O_4," *IEEE J. Quantum Electron.*, vol. QE-22, no. 7, pp. 1013–1014, Jul. 1986.

[6] L. E. Myers, R. C. Eckardt, M. M. Fejer, R. L. Byer, W. R. Bosenberg, and J. W. Pierce, "Quasi-phase-matched optical parametric oscillators in bulk periodically poled $LiNbO_3$," *J. Opt. Soc. Amer. B*, vol. 12, no. 11, pp. 2102–2116, Nov. 1995.

[7] J. D. Bierlein and H. Vanherzeele, "Potassium titanyl phosphate—Properties and new applications," *J. Opt. Soc. Amer. B*, vol. 6, no. 4, pp. 622–633, Apr. 1989.

[8] U. Heitmann, M. Kotteritzsch, S. Heitz, and A. Hese, "Efficient generation of tunable VUV laser-radiation below 205 nm by SFM in BBO," *Appl. Phys. B*, vol. 55, no. 5, pp. 419–423, Nov. 1992.

[9] H. P. Wagner, "Second-harmonic generation in thin film II-VI optical waveguides," *Phys. Stat. Sol. B*, vol. 187, no. 2, pp. 363–369, Feb. 1995.

[10] H. P. Wagner, S. Wittmann, H. Schmitzer, and H. Stanzl, "Phase-matched second harmonic generation using thin film ZnTe optical waveguides," *Appl. Phys.*, vol. 77, no. 8, pp. 3637–3640, Apr. 1995.

[11] S. Janz, C. Fernando, H. Dai, F. Chatenoud, M. Dion, and R. Normandin, "Quasi-phase-matched second-harmonic generation in reflection from $Al_x Ga_{1-x}As$ heterostructures," *Opt. Lett.*, vol. 18, no. 8, pp. 589–591, Apr. 1993.

[12] M. Cada, M. Svilans, S. Janz, R. Bierman, R. Normandin, and J. Glinski, "Second harmonic generation in InGaAsP waveguides at 1.3 μm wavelength," *Appl. Phys. Lett.*, vol. 61, no. 17, pp. 2090–2092, Oct. 1992.

[13] J. H. Marsh, "Quantum-well intermixing," *Semicond. Sci. Tech.*, vol. 8, no. 6, pp. 1136–1155, Jun. 1993.

[14] B. Ryvkin, K. Panajotov, A. Georgievski, J. Danckaert, M. Peeters, G. Verschaffelt, H. Thienpont, and I. Veretennicoff, "Effect of photon-energy-dependent loss and gain mechanisms on polarization switching in vertical-cavity surface-emitting lasers," *J. Opt. Soc. Amer. B*, vol. 16, no. 11, pp. 2106–2113, Nov. 1999.

[15] A. Tredicucci, C. Gmachl, F. Capasso, D. L. Sivco, A. L. Hutchinson, and A. Y. Cho, "Long wavelength superlattice quantum cascade lasers at lambda similar or equal to 17 μm," *Appl. Phys. Lett.*, vol. 74, no. 5, pp. 638–640, Feb. 1999.

[16] N. Nunoya, M. Nakamura, M. Morshed, S. Tamura, and S. Arai, "High-performance 1.55 μm wavelength GaInAsP-InP distributed-feedback lasers with wirelike active regions," *IEEE J. Sel. Top. Quantum Electron.*, vol. 7, no. 2, pp. 249–258, Mar. 2001.

[17] M. Aoki, M. Suzuki, H. Sano, T. Kawano, T. Ido, T. Taniwatari, K. Uomi, and A. Takai, "InGaAs/InGaAsP MQW electroabsorption modulator integrated with a DFB laser fabricated by band-gap energy control selective-area MOCVD," *IEEE J. Quantum Electron.*, vol. 29, no. 6, pp. 2088–2096, Jun. 1993.

[18] P. Doussiere, P. Garabedian, C. Graver, D. Bonnevie, T. Fillion, E. Derouin, M. Monnot, J. G. Provost, D. Leclerc, and M. Klenk, "1.55 μm polarization-independent semiconductor optical amplifier with 25-DB fiber to fiber gain," *IEEE Photon. Tech. Lett.*, vol. 6, no. 2, pp. 170–172, Feb. 1994.

[19] T. L. Koch and U. Koren, "Semiconductor photonic integrated-circuits," *IEEE J. Quantum Electron.*, vol. 27, no. 3, pp. 641–653, Mar. 1991.

[20] A. S. Helmy, "Phase matching using Bragg reflection waveguides for monolithic nonlinear optics applications," *Opt. Exp.*, vol. 14, no. 3, pp. 1243–1252, Feb. 2006.

[21] M. M. Choy and R. L. Byer, "Accurate second-order susceptibility measurements of visible and infrared nonlinear crystals," *Phys. Rev. B*, vol. 14, no. 4, pp. 1693–1706, Aug. 1976.

[22] A. Fiore, V. Berger, E Rosencher, P. Bravetti, and J. Nagle, "Phase matching using an isotropic nonlinear optical material," *Nature*, vol. 391, no. 6666, pp. 463–466, Jan. 1998.

[23] K. Moutzouris, S. V. Rao, M. Ebrahimzadeh, A. De Rossi, M. Calligaro, V. Ortiz, and V. Berger, "Second-harmonic generation through optimized modal phase matching in semiconductor waveguides," *Appl. Phys. Lett.*, vol. 83, no. 4, pp. 620–622, Jul. 2003.

[24] J. S. Aitchison, M. W. Street, N. D. Whitbread, D. C. Hutchings, J. H. Marsh, G. T. Kennedy, and W. Sibbett, "Modulation of the second-order nonlinear tensor components in multiple-quantum-well structures," *IEEE J. Sel. Top. Quantum Electron.*, vol. 4, no. 4, pp. 695–700, Jul. 1998.

[25] E. D. Palik, *Handbook of Optical Constants of Solids*. Orlando, FL: Academic, 1985.

[26] P. Yeh and A. Yariv, "Bragg reflection waveguides," *Opt. Commun.*, vol. 19, no. 3, pp. 427–430, Dec. 1976.

[27] P. Ye, A. Yariv, and C. S. Hong, "Electromagnetic propagation in periodic stratified media .I. general theory," *J. Opt. Soc. Amer.*, vol. 67, no. 4, pp. 423–438, Apr. 1977.

[28] S. R. A. Dods, "Bragg reflection waveguide," *J. Opt. Soc. Amer. A*, vol. 6, no. 9, pp. 1465–1476, Sep. 1989.

[29] E. Simova and I. Golub, "Polarization splitter/combiner in high index contrast Bragg reflector waveguides," *Opt. Exp.*, vol. 11, no. 25, pp. 3425–3430, Dec. 2003.

[30] A. Mizrahi and L. Schachter, "Optical Bragg accelerators," *Phys. Rev. E*, vol. 70, no. 1, pp. 016505-1–016505-21, Jul. 2004.

[31] A. Mizrahi and L. Schachter, "Bragg reflection waveguides with a matching layer," *Opt. Exp.*, vol. 12, no. 14, pp. 3156–3170, Jul. 2004.

[32] C. Wchter, F. Lederer, L. Leine, U. Trutschel, and M. Mann, "Nonlinear Bragg reflection waveguide," *J. Appl. Phys.*, vol. 71, no. 8, pp. 3688–3692, Apr. 1992.

[33] P. M. Lambkin and K. A. Shore, "Nonlinear semiconductor Bragg reflection waveguide structures," *IEEE J. Quantum Electron.*, vol. 27, no. 3, pp. 824–829, Mar. 1991.

[34] B. R. West and A. S. Helmy", "Properties of the quarter-wave Bragg reflection waveguide: theory," *J. Opt. Soc. Amer. B*, vol. 23, no. 6, pp. 1207–1220, Jun. 2006.

[35] P. Abolghasem, J. Han, B. J. Bijlani, A. Arjmand, and A. S. Helmy, "Highly efficient second-harmonic generation in monolithic matching layer enhanced $Al_x Ga_{1-x}As$ Bragg reflection waveguides," *IEEE Photon. Tech. Lett.*, vol. 21, no. 19, pp. 1462–1464, Oct. 2009.

[36] P. Abolghasem and A. S. Helmy, "Matching layers in Bragg reflection waveguides for enhanced nonlinear interaction," *IEEE J. Quantum Electron*, vol. 45, no. 5–6, pp. 646–653, May 2009.

[37] P. Abolghasem, J. Han, B. J. Bijlani, and A. S. Helmy, "Type-0 second order nonlinear interaction in monolithic waveguides of isotropic semiconductors," *Opt. Exp.*, vol. 18, no. 12, pp. 12681–12689, Jun. 2010.

[38] J. P. Bouchard, M. Tetu, S. Janz, D. X. Xu, Z. R. Wasilewski, P. Piva, U. G. Akano, and I. V. Mitchell, "Quasi-phase matched second-harmonic generation in an $Al_x Ga_{1-x}As$ asymmetric quantum-well waveguide using ion-implantation-enhanced intermixing," *Appl. Phys. Lett.*, vol. 77, no. 26, pp. 4247–4249, Dec. 2000.

[39] C. Langrock, E. Diamanti, R. V. Roussev, Y. Yamamoto, M. M. Fejer, and H. Takesue, "Highly efficient single-photon detection at communication wavelengths by use of upconversion in reverse-proton-exchanged periodically poled $LiNbO_3$ waveguides," *Opt. Lett.*, vol. 30, no. 13, pp. 1725–1727, Jul. 2005.

[40] M. Fujimura, H. Okabe, K. Beniya, and T. Suhara, "Waveguide quasi-phase-matched sum-frequency generation device pumped by InGaAs laser diode for single-photon detection in communication wavelength band," *Jpn. J. Appl. Phys.*, vol. 46, no. 9A, pp. 5868–5870, Sep. 2007.

[41] T. Kanada and D. L. Franzen, "Optical wave-form measurement by optical-sampling with a mode-locked laser diode," *Opt. Lett.*, vol. 11, no. 1, pp. 4–6, Jan. 1986.

[42] S. Kawanishi, "Ultrahigh-speed optical time-division-multiplexed transmission technology based on optical signal processing," *IEEE J. Quantum Electron.*, vol. 34, no. 11, pp. 2064–2079, Nov. 1998.

[43] J. Han, P. Abolghasem, B. J. Bijlani, and A. S. Helmy, "Continuous-wave sum-frequency generation in AlGaAs Bragg reflection waveguides," *Opt. Lett.*, vol. 34, no. 23, pp. 3656–3658, Dec. 2009.

[44] R. V. Roussev, C. Langrock, J. R. Kurz, and M. M. Fejer, "Periodically poled lithium niobate waveguide sum-frequency generator for efficient single-photon detection at communication wavelengths," *Opt. Lett.*, vol. 29, no. 13, pp. 1518–1520, Jul. 2004.

[45] P. Abolghasem, M. Hendrych, X. Shi, J. P. Torres, and A. S. Helmy", "Bandwidth control of paired photons generated in monolithic Bragg reflection waveguides," *Opt. Lett.*, vol. 34, no. 13, pp. 2000–2002, Jul. 2009.

[46] P. Bravetti, A. Fiore, V. Berger, E. Rosencher, J. Nagle, and O. Gauthier-Lafaye, "5.2–5.6 μm source tunable by frequency conversion in a GaAs-based waveguide," *Opt. Lett.*, vol. 23, no. 5, pp. 331–333, Mar. 1998.

[47] D. Zheng, L. A. Gordon, Y. S. Wu, R. S. Feigelson, M. M. Fejer, R. L. Byer, and K. L. Vodopyanov, "16 μm infrared generation by difference-frequency mixing in diffusion-bonded-stacked GaAs," *Opt. Lett.*, vol. 23, no. 13, pp. 1010–1012, Jul. 1998.

[48] K. L. Vodopyanov and Y. H. Avetisyan, "Optical terahertz wave generation in a planar GaAs waveguide," *Opt. Lett.*, vol. 33, no. 20, pp. 2314–2316, Oct. 2008.

[49] J. B. Han, P. Abolghasem, D. Kang, B. J. Bijlani, and A. S. Helmy, "Difference-frequency generation in AlGaAs Bragg reflection waveguides," *Opt. Lett.*, vol. 35, no. 14, pp. 2334–2336, Jul. 2010.

[50] J. B. Han, D. P. Kang, P. Abolghasem, B. J. Bijlani, and A. S. Helmy, "Pulsed- and continuous-wave difference-frequency generation in AlGaAs Bragg reflection waveguides," *J. Opt. Soc. Amer. B*, vol. 27, no. 12, pp. 2334–2488-2494, Dec. 2010.

[51] B. J. Bijlani and A. S. Helmy, "Bragg reflection waveguide diode lasers," *Opt. Lett.*, vol. 34, no. 23, pp. 3734–3736, Dec. 2009.
[52] C. Tong, B. J. Bijlani, S. Alali, and A. S. Helmy, "Characteristics of Edge-Emitting Bragg Reflection Waveguide Lasers," *IEEE J. Quantum Electron.*, vol. 46, no. 11, pp. 1605–1610, Nov. 2010.
[53] Genia Photonics Inc. (2010). [Online]. Available: www.geniaphotonics.com
[54] T. Suhara and M. Fujimura, *Waveguide Nonlinear-Optic Devices*. New York: Springer-Verlag, 2003.
[55] R. C. Miller, "Optical second-harmonic generation in piesoelectric crystals (ferroelectrics KH_2PO_4, KD_2PO_4, $NH_4H_2PO_4$, KH_2AsO_4, quartz, $AlPO_4$, ZnO, CdS, GaP, GaAs, $BaTiO_3$; T/E)," *Appl. Phys. Lett.*, vol. 5, no. 1, pp. 17–19, Jul. 1964.
[56] M. Ohashi, T. Kondo, R. Ito, S. Fukatsu, Y. Shiraki, K. Kumata, and S. S. Kano, "Determination of quadratic nonlinear optical coefficient of $Al_xGa_{1-x}As$ system by the method of reflected second harmonics," *J. Appl. Phys.*, vol. 74, no. 1, pp. 596–601, Jul. 1993.
[57] T. Kondo and I. Shoji, "Study on wavelength conversion by compound-semiconductor-based quasi phase-matching devices," *Photon. Based Wavelength Integr. Manipul.*, vol. 2, pp. 151–160, 2005.
[58] P. N. Butcher and D. Cotter, *The Elements of Nonlinear Optics*. Cambridge, UK: Cambridge Univ. Press, 1990.
[59] S. J. B. Yoo, R. Bhat, C. Caneau, and M. A. Koza, "Quasi-phase-matched second-harmonic generation in AlGaAs waveguides with periodic domain inversion achieved by wafer-bonding," *Appl. Phys. Lett.*, vol. 66, no. 25, pp. 3410–3412, Jun. 1995.
[60] A. S. Helmy, B. J. Bijlani, and P. Abolghasem, "Phase matching in monolithic Bragg reflection waveguides," *Opt. Lett.*, vol. 32, no. 16, pp. 2399–2401, Aug. 2007.
[61] P. Abolghasem, J. Han, B. J. Bijlani, A. Arjmand, and A. S. Helmy, "Continuous-wave second harmonic generation in Bragg reflection waveguides," *Opt. Exp.*, vol. 17, no. 11, pp. 9460–9467, May 2007.
[62] T. Suhara, H. Ishizuki, M. Fujimura, and H. Nishihara, "Waveguide quasi-phase-matched sum-frequency generation device for high-efficiency optical sampling," *IEEE Photon. Tech. Lett.*, vol. 11, no. 8, pp. 1027–1029, Aug. 1999.
[63] J. S. Aitchison, D. C. Hutchings, J. U. Kang, G. I. Stegeman, and A. Villeneuve, "The nonlinear optical properties of AlGaAs at the half band gap," *IEEE J. Quantum. Electron.*, vol. 33, no. 3, pp. 341–348, Mar. 1997.
[64] M. Sheikbahae, D. C. Hutchings, D. J. Hagen, and E. W. Vanstryland, "Dispersion of bound electronic nonlinear refraction in solids," *IEEE J. Quantum. Electron.*, vol. 27, no. 6, pp. 1296–1309, Jun. 1991.
[65] J. B. Han, P. Abolghasem, B. J. Bijlani, A. Arjmand, S. C. Kumar, A. Esteban-Martin, M. Ebrahim-Zadeh, and A. S. Helmy, "Femtosecond second-harmonic generation in AlGaAs Bragg reflection waveguides: Theory and experiment," *J. Opt. Soc. Amer. B*, vol. 27, no. 6, pp. 1291–1298, Jun. 2010.

Payam Abolghasem received the B.A.Sc. degree from the University of Ottawa, Ottawa, ON, Canada, in 2004, the M.A.Sc. degree from McMaster University, Hamilton, ON, Canada, in 2006 and the Ph.D. degree from the University of Toronto, Toronto, ON, in 2011, all in electrical engineering.

He is currently a Ministry of Research and Innovation (MIR) Postdoctoral Fellow at the Department of Electrical and Computer Engineer, University of Toronto. His research interests are in optical frequency mixing in semiconductors, on-chip integrated parametric devices, semiconductor diode lasers, and UV-IR optoelectronics.

Jun-Bo Han received the B.Sc. and Ph.D. degrees from Wuhan University, Wuhan, China, in 2002 and 2007, respectively.

He is currently an Associate Professor in the Wuhan National High Magnetic Field Center, Huazhong University of Science and Technology after he finished his postdoctoral research in the Photonics Group of the University of Toronto in 2010. Prior to his academic career, he held a position at the Wuhan R&D Center of Delta Electronics in China between 2007 and 2008.

Dongpeng Kang received the B.Sc. degree in physics in 2006 and the M.Sc. degree in optics in 2008, both from the Harbin Institute of Technology, Harbin, China. He is now working toward the Ph.D. degree in electrical and computer engineering at the University of Toronto, Toronto, ON, Canada.

His current research is on the nonlinear and quantum optical properties of III-V semiconductor waveguides.

Bhavin J. Bijlani received the undergraduate degree in engineering science from the University of Toronto, Toronto, ON, Canada and the Ph.D. degree from the Photonics Group of the Electrical and Computer Engineering Department, University of Toronto. His thesis research was on nonlinear frequency conversion and diode lasers in semiconductor Bragg Reflection Waveguides.

Currently, he is an Optoelectronics Device Engineer at Onechip Photonics.

Amr S. Helmy received the B.Sc. degree in electronics and telecommunications engineering from Cairo University, Giza, Egypt, in 1993, and the M.Sc. and Ph.D. degrees from the University of Glasgow, Glasgow, U.K. with a focus on photonic fabrication technologies, in 1994 and 1999, respectively.

He is currently an Associate Professor in the Department of Electrical and Computer Engineering at the University of Toronto, Toronto, ON, Canada. Prior to his academic career, he held a position at Agilent Technologies Photonic Devices, R&D Division, U.K. between 2000 and 2004. At Agilent his responsibilities included developing distributed feedback lasers, monolithically integrated lasers, modulators, and amplifiers in InP-based semiconductors. He also developed high-powered submarine-class 980 nm InGaAs pump lasers. His research interests include photonic device physics and characterization techniques, with emphasis on nonlinear optics in III-V semiconductors; applied optical spectroscopy in III-V optoelectronic devices and materials; III-V fabrication and monolithic integration techniques.

Dr. Helmy has been awarded the Francis Morrison Award from the University of Glasgow for his graduate studies. In 2007, he was awarded an Early Researcher Award from the Ministry of Research and Innovation in Ontario-Canada for his leading work on nonlinear frequency conversion in III-V semiconductors. He is a member of the Optical Society of America. He has served as the Chair of the nano-technology sub-committee in the IEEE Communications Society since 2005, as the Associate Editor - Canada for the IEEE Laser and Electro-Optics Society News Letter since 2006 and is currently the Chair of the Optical Materials and Processing sub-committee for the same society. He has also served as VP membership for the IEEE LEOS between 2007 and 2010.